Viability of Xenotime-Type Rare Earth Orthophosphates as High-Temperature Environmental Barrier Coatings

Imoen Hawthorne[1] and Elizabeth Opila[1,2]

1. Materials Science and Engineering, University of Virginia, United States
2. Mechanical and Aerospace Engineering, University of Virginia, United States

Abstract

Conventional environmental barrier coatings (EBCs), used for the protection of SiC-based ceramic matrix composites (SiC-CMCs) in aero turbine engines, are primarily comprised of Yb disilicates (YbDS). In an effort to make more inexpensive and environmentally friendly coatings, rare earth orthophosphate ($REPO_4$) containing mineral, xenotime, is being investigated. Four naturally occurring minerals were used to determine a composition of $(Y_{0.08}Gd_{0.04}Dy_{0.07}Er_{0.05}Yb_{0.04})PO_4$. Phase pure mineral-synthetic $REPO_4$, an equimolar mixture of the five rare earth elements (REE), and the individual REE were densified by spark plasma sintering. CMAS exposures at 1300°C showed an improvement to YbDS through the formation of a complex reaction product layer which temporarily inhibits the infiltration of residual CMAS. Additionally, high-temperature high-velocity steam exposures showed parabolic reaction product growth rates similar to YbDS for most $REPO_4$ species and a significantly longer incubation time. Xenotime-type $REPO_4$ have demonstrated capacity to be viable EBC candidates in SiC-CMC systems.

1. Introduction

In order to make a more efficient aero turbine engine, there must be an increase in operating temperature or reduction of weight. One method that can be implemented is moving away from conventional Ni superalloys and towards SiC-ceramic matrix composites (SiC-CMCs). SiC-CMCs have been proposed due to having higher melting temperatures, better high-temperature creep resistance, and lower density compared to conventional Ni superalloys[1,2]. However, SiC-CMCs react with combustion products and excess oxygen reacting with SiC to form SiO_2 with concurrent oxide volatilization[3–5].

Environmental barrier coatings (EBCs) are implimented to limit silica volatility, extending the service lifetime of the part. EBCs must be resistant to steam[6–8], calcium-magnesium-aluminum silicates (CMAS)[9,10], have a coefficient of thermal expansion (CTE) match with SiC, have high phase stability, and minimal reactivity with the Si bond coat and SiC substrate it is protecting[11,12]. Conventional EBCs are a two-layer design containing a Si bond coat and $RE_2Si_2O_7$ (rare earth disilicates REDS) as a protective outer layer. REDS reduce the rate of SiC oxidation and volatility in water-vapor environments[7,9,13–16]. Operating temperature of the EBC system will then be limited by the Si bond coat at 1414°C due to the melting temperature of Si[17,18]. The Si bond coat will also thermally oxidize to form SiO_2 which will volatize when in a steam rich environment[12,14–16,19,20].

Xenotime minerals are naturally forming and can be found throughout the world as a source of rare earth orthophosphates ($REPO_4$)[21–28]. These are defined by mineralogists as YPO_4-type minerals, but are actually multicomponent $REPO_4$ where RE = Y, Tb-Lu[24,26,29]. Mineral compositions have been determined from seven minerals to be $(Y_{0.72}Nd_{0.01}Sm_{0.02}Gd_{0.04}Tb_{0.01}Dy_{0.07}Ho_{0.01}Er_{0.04}Tm_{0.01}Yb_{0.06})PO_4$[25,30]. The mineral is primarily Y with minor amounts of Gd, Dy, Er, Yb, and trace amounts of Nd, Sm, Tb, Tm. Multicomponent materials with xenotime-type structure have been synthesized[21,23,24,31–33] including as many as seven

components[32], but these multicomponent $REPO_4$ are typically equimolar compositions instead of mineral-synthetic. It is important to note that La-Tb have monazite-type structures which are monoclinic granting different properties[34].

$YbPO_4$ has shown promise as an EBC[35,36]. When exposed to high-velocity high-temperature water vapor at 1400°C, Yb_2O_3 forms at slower parabolic reaction rates than the formation of Yb_2SiO_5 (Yb monosilicate YbMS) in YbDS systems. CMAS exposures at 1300°C showed the formation of a tri-layer reaction product which inhibits the infiltration of CMAS into the bulk material. Similar results have been observed in low-velocity water vapor at 1350°C. CMAS resistance was also observed at 900°C[28]. $YbPO_4$ and YPO_4 do not react or decompose when exposed to SiO_2 indicating chemical compatability with Si-based substrates[28,36]. CTE values for xenotime-type $REPO_4$ have shown reasonable match with SiC-CMCs[32,36]. Investigation into multi-component $REPO_4$ has shown similar properties to that of single component $REPO_4$ with the formation of RE_2O_3 when exposed to high-temperature water vapor[37] and the formation of $Ca_8MgRE(PO_4)_7$ when exposed to CMAS[38–41]. These properties indicate that xenotime-type $REPO_4$ show promise as an EBC.

Multicomponent RE-containing are typically prepared using mixtures of RE_2O_3 powders[23,32,35,36,38]. Synthesis of single RE-containing compounds require the separation of RE elements from natural forming minerals, such as xenotime, which currently require 60 steps of soaking in strong acids and strong bases to separate Yb and Lu[26,42]. The recombination of single component RE-compounds to multicomponent to improve properties is a costly and environmentally unfriendly process that can be mitigated by utilizing the natural multicomponent composition of RE-containing minerals, like xenotime. This report seeks to evaluate thermophysical and thermochemical properties of xenotime-type $REPO_4$ through characterizing minerals, xenotime-mineral-synthetic $REPO_4$, and single component $REPO_4$ to evaluate the capability of xenotime minerals as a cost-effective and environmentally friendly alternative to REDS EBCs.

2. Methods

Four xenotime minerals were obtained from throughout the world (Brazil, Democratic Republic of the Congo, Norway, and Pakistan) and were polished to 1 μm and sputter coated with Au-Pd. Elemental composition was determined using energy dispersive spectroscopy (EDS).

Y, Gd, Dy, Er, and Yb were identified from the xenotime minerals were selected as candidate $REPO_4$. These $REPO_4$ were then synthesized using a co-precipitation method described by Ridley, et al.[36] using RE_2O_3 and H_3PO_4 in H_2O. The resulting $REPO_4$ is hydrated so the product was calcined at 900°C for 8h. The product was then ball milled using ZrO_2 milling media for at least 24h and phase purity was confirmed using X-ray Diffraction (XRD). The used multicomponent $REPO_4$ are not listed in the International Centre for Diffraction Data (ICDD) database, but have the same tetragonal crystal structure as YPO_4 with minor lattice parameter shifts, so phase purity can be determined by the exclusion of additional peaks from the single components.

$REPO_4$ were densified using spark plasma sintering (SPS DCS 25-10, Thermal Technologies) with a 30 min hold at 1500°C 65 MPa. Densified pucks were annealed at 1500°C in a box furnace for 30h. Samples were then cut to 10 mm x 10 mm x 3 mm coupons and polished to 1 μm. These polished coupons were used for high-temperature high-velocity water vapor and high-temperature CMAS tests.

CMAS resistance of $REPO_4$ species was determined using $33CaO\text{-}9MgO\text{-}13AlO_{1.5}\text{-}45SiO_2$ CMAS (UCSB) used by Kramer et al[43]. The oxides were weighed out, mixed, and heated to 1500°C in a

box furnace to form a molten glass. The molten glass was then quenched in water and crushed into a fine powder using a mortar and pestle. CMAS powder was pressed into pellets with a mass of 40 mg using a hydraulic press and were sintered at 1100°C for 6h. Pellets were placed on the polished coupons to obtain a CMAS loading of 40 mg cm^{-2} which allowed for the comparison of $REPO_4$ to other materials[13,36]. CMAS-loaded samples were placed into a box furnace and exposed to 1300°C lab air with exposure times of 4, 24, and 96h. Heating and cooling rates were controlled at 5°C min^{-1}. After exposure, coupons were characterized with XRD to observe any crystalline reaction products. FEI Quanta 650 scanning electron microscope (SEM) was used to take plan view images which were stitched to allow for observations of the CMAS melt pool dimensions. Cross section micrographs were taken to characterize the reaction product thickness and sample recession. Elemental composition of reaction product layer was also evaluated using EDS.

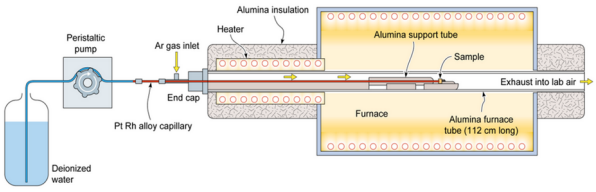

Figure 1: Diagram of modified horizontal tube furnace to create high-temperature, high-velocity water vapor[52]

Water vapor resistance of $REPO_4$ species was determined using the high-temperature, high-velocity steam jet shown in Figure 1. Samples were placed on a Pt foil lined aluminum boat and secured with Pt wire to be at a 45°angle and spaced 1 mm away from the exit of the Pt-Rh capillary. The furnace was flushed with flowing Ar and heated to 1400°C. Deionized water flows through the capillary through a pre-heater and into the furnace creating a gas which impinges the sample at a gas flow gradient of 100-250 m s^{-1}[7]. The steam jet system simulates the high-temperature, high-velocity water vapor product found inside a turbine engine. Three separate samples per composition were exposed for 72, 120, and 240 h. Reaction products of exposed samples were characterized by XRD and plan view SEM. Micrographs were stitched together to construct a map of the surface to characterize surface variations as a function of steam velocity. Samples were then cross sectioned to measure reaction product thickness using SOFIA, an open-source tool for measuring thickness of reaction products[6,44,45].

3. Results

Composition of xenotime minerals are shown in Table 1 and Figure 2. The average composition of xenotime minerals is determined to be $(Y_{0.08}Gd_{0.04}Dy_{0.07}Er_{0.05}Yb_{0.04})PO_4$ indicating there are five REE cations in a multicomponent mixture. The compositions of all four mineral species were found to be similar as graphically shown in Figure 2, presumably dictated by the natural abundance of REE in the Earth's crust with the mineral comprised of Y at an order of magnitude more abundant than Gd, Dy, Er, and Yb and two orders of magnitude more abundant than the trace elements, Nd, Ho, and Tm observed in previous studies[30,46–48].

Table 1: Summary of composition of rare earth elements in xenotime minerals from Brazil, Democratic Republic of the Congo, Norway, and Pakistan determined by energy dispersive spectroscopy

	RE (%)	Y	Gd	Dy	Er	Yb
Brazil	22	0.79	0.05	0.09	0.04	0.02
Congo	22.7	0.79	0.04	0.08	0.05	0.05
Norway	18.1	0.81	0.04	0.07	0.04	0.04
Pakistan	23.4	0.80	0.04	0.08	0.05	0.03

Mean	-	0.80	0.04	0.08	0.05	0.04
Model	**-**	**0.8**	**0.04**	**0.07**	**0.05**	**0.04**

SEM characterization of the minerals show impurities, such as TiO_2 in the mineral from Brazil and SiO_2 in the mineral from Democratic Republic of the Congo and Pakistan.

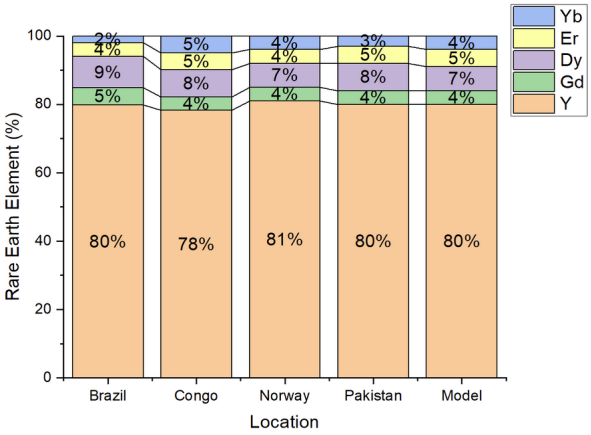

Figure 2: Summary of compositions of rare earth elements in xenotime minerals from throughout the world determined by energy dispersive spectroscopy

Examples of phase pure XRD data are shown in Figure 3. $GdPO_4$ is observed to be monazite-type monoclinic while the rest of the compounds are xenotime-type tetragonal, as expected. Peaks for the single component $REPO_4$ match those found in the ICDD database and the peaks for the multicomponent are narrow implying the RE cations including Gd are well mixed.

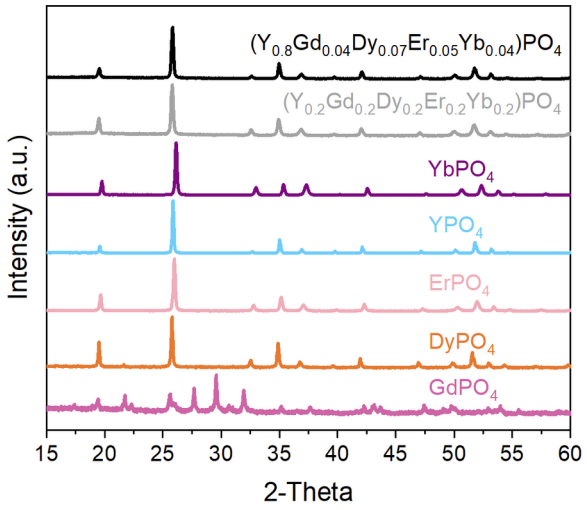

Figure 3: XRD responses of mineral-synthetic $REPO_4$, equimolar, and single component RE = Yb, Y, Er, Dy, Gd

Cross section micrographs of $ErPO_4$ specimens exposed to 1300°C CMAS are shown in Figure 5. Reaction products are observed in all three exposure times, but the residual CMAS is only present at 4h. The primary reaction product has been previously reported as $Ca_8MgRE(PO_4)_7$[36,38,39,41,49]. For multicomponent $REPO_4$, similar results were shown with reaction product REE content being identical to the bulk material. Rounding of the reaction product and localized blistering of the $REPO_4$ is observed at longer exposure times as shown for $ErPO_4$ in Figure 4.

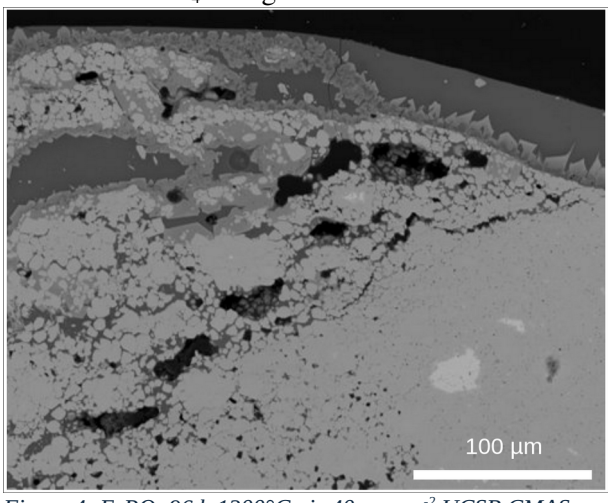

Figure 4: $ErPO_4$ 96 h 1300°C air 40 mg cm^{-2} UCSB CMAS

High-temperature, high-velocity water vapor exposures result in the formation of RE_2O_3

and multiple intermediate phases depending on the REE composition. For $YbPO_4$ only RE_2O_3 is observed to form, but the intermediate phases are observed to change as the REE cation size gets larger as observed in Figure 6. These intermediate phases are difficult to observe with concentric backscatter SEM as shown in Figure 5, but become more apparent with EDS linescans and wavelength dispersive spectroscopy (WDS), not shown. Similarly, as shown in the CMAS exposures, no REE is favored in any of the reaction products for the multicomponent $REPO_4$.

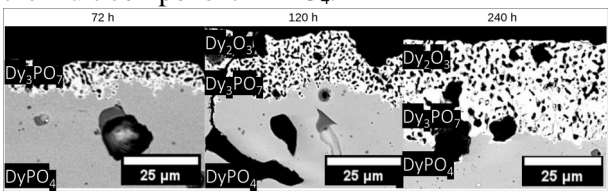

Figure 5: Reaction product evolution of $DyPO_4$ exposed to 1400°C steam at 200-250 m s^{-1} for 72, 120, and 240h

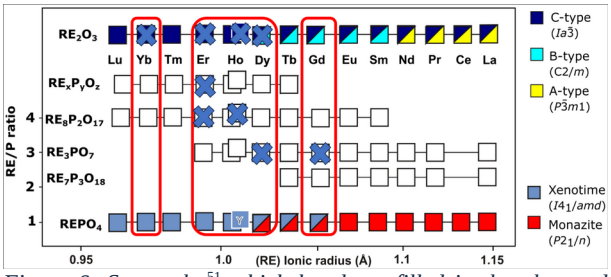

Figure 6: Serra plot[51] which has been filled in the observed intermediate phases for single component $REPO_4$

Steam reaction kinetics of YbDS and $REPO_4$ species are reported in Figure 7. It is observed that the formation of the reaction product follows a parabolic growth rate indicating that the reaction products act as a diffusion barrier for the effluence of a P-O-H vapor species similar to how YbMS inhibits the effluence of $Si(OH)_4$ in conventional YbDS[6]. The incubation time for most of the $REPO_4$ species is observed to be longer than that of YbDS, with the exception of $ErPO_4$ which shows no incubation time. The parabolic reaction kinetics for the $REPO_4$ species with the exception of YPO_4 are observed to be similar to YbDS.

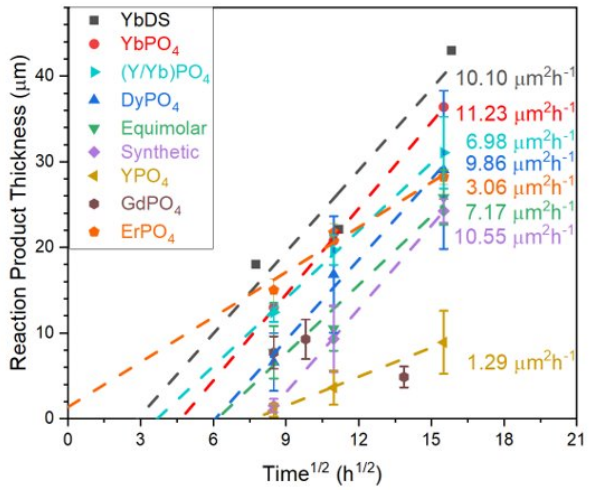

Figure 7 Net reaction product thickness measurements of various $REPO_4$ species and YbDS exposed to 200-250 m/s 1400°C water vapor plotted against $h^{1/2}$

4. Discussion

$ErPO_4$ shows an improved resistance to CMAS compared to YbDS. At all exposure times there is the presence of a dense reaction product layer that inhibits the infiltration of CMAS. However, the presence of this reaction product layer does not indicate immunity to infiltration as two breakdown blisters are observed on the edges of the residual CMAS dome. The breakdown could be associated with the depletion of CaO in the edge of the residual CMAS as CaO is a major constituent in the reaction product layer. The inability for the reaction product to form results in the growth of Al_2O_3 and REDS dendrites which grow from the $Ca_8MgRE(PO_4)_7$ reaction product. The dendrites create gaps in the $Ca_8MgRE(PO_4)$ layer allowing for infiltration of the residual CMAS along the grain boundaries which then react with the unprotected $REPO_4$ to blister and repeat the process until the CMAS is depleted or there is complete infiltration. There is a critical length of time at 1300°C before the breakdown occurs as the thickness of the reaction product at the center of the sample is observed to be the same thickness for both 24 and 96h. $REPO_4$ do not offer complete protection from CMAS, but they still demonstrate a significant improvement over the rapid infiltration of CMAS resulting in coating failure seen in YbDS[36].

High-temperature high-velocity steam exposure of $REPO_4$ species results in the formation of porous layers of various $RE_xP_yO_z$ intermediate species. The intermediate phases, detected by EDS linescans, show a loose correlation with REE cation size with smallest-tested-cation Yb only forming

Yb_2O_3 and larger cations forming multiple rare earth oxyphosphates with increasing RE:P ratios for smaller RE cation radius. Multicomponent $REPO_4$ show the formation of intermediate phases consistent with $RE_{14}P_4O_{31}$[50] and RE_5PO_{10} which have not been observed in previous steam resistance studies of $REPO_4$. The formation of the intermediate phases traverses the Y_2O_3-P_2O_5 phase diagram as the P-O-H vapor species is removed following a diffusion limited process. The formation of multiple intermediate phases could be the the explanation for the longer incubation time for the different $REPO_4$ species. However, the parabolic growth rates are not solely linked to cation radius as YPO_4 shows the slowest formation of reaction product despite not being the largest or smallest REE cation.

5. Conclusion

Thermochemical properties of xenotime-type $REPO_4$ species suggest promise for the application of xenotime minerals as EBCs. Phase pure $REPO_4$ species were synthesized using H_3PO_4 and RE_2O_3. Molten CMAS exposures results in the formation of a semi-protective layer that compares favorably to YbDS. Exposure to high-temperature high-velocity steam results in the formation of RE oxyphosphates such as $RE_{14}P_4O_{31}$ and RE_5PO_{10} which grow following a parabolic growth rate indicating diffusion-limited outward transport of a volatile P-O-H compound through the porous reaction products. For most $REPO_4$ species, the reaction product growth rates match that of YbDS under similar conditions. Both CMAS and steam exposures demonstrate an improvement in environmental resistance compared to YbDS indicating that xenotime-type $REPO_4$ are promising candidates for next-generation EBCs. Use of xenotime minerals as a source of $REPO_4$ for EBCs could lead to more cost-effective materials processing and reduced environmental impact by avoiding complex REE separation routes.

Acknowledgement

The authors acknowledge funding from Dr. Daniel Cole, program manager, US Army Research Office under ARO Cooperative Agreement Number W911NF-22-2-0022 and W911NF-23-2-0145. Additional thanks to the Virginia Space Grant Consortium for project funding. The authors would also like to acknowledge the Nanoscale Materials Characterization Facility (NMCF) at the University of Virginia for supporting this research through access to characterization equipment.

References

1. CARTER, C. H., DAVIS, R. F. & BENTLEY, J. Kinetics and Mechanisms of High-Temperature Creep in Silicon Carbide: II, Chemically Vapor Deposited. *J. Am. Ceram. Soc.* **67**, 732–740 (1984).
2. Farhat, H. *Operation, Maintenance, and Repair of Land-Based Gas Turbines*. *Operation, Maintenance, and Repair of Land-Based Gas Turbines* (Elsevier, 2021). doi:10.1016/B978-0-12-821834-1.09991-3.
3. Opila, E. J. & Hann, R. E. Paralinear oxidation of CVD SiC in water vapor. *J. Am. Ceram. Soc.* **80**, 197–205 (1997).
4. Opila, E. J. & Jacobson, N. S. Oxidation and Corrosion of Ceramics. in *Ceramics Science and Technology* vol. 4 1–93 (Wiley, 2013).
5. Jacobson, N. S., Opila, E. J., Myers, D. L. & Copland, E. H. Thermodynamics of gas phase species in the Si-O-H system. *J. Chem. Thermodyn.* **37**, 1130–1137 (2005).
6. Kane, K. *et al.* Evaluating steam oxidation kinetics of environmental barrier coatings. *J. Am. Ceram. Soc.* **105**, 590–605 (2022).
7. Ridley, M. & Opila, E. Thermochemical stability and microstructural evolution of Yb2Si2O7 in high-velocity high-temperature water vapor. *J. Eur. Ceram. Soc.* **41**, 3141–3149 (2021).
8. Ridley, M. & Opila, E. Variable thermochemical stability of RE2Si2O7 (RE = Sc, Nd, Er, Yb, or Lu) in high-temperature high-velocity steam. *J. Am. Ceram. Soc.* **105**, 1330–1342 (2022).
9. Guo, X. *et al.* High-entropy rare-earth disilicate (Lu0.2Yb0.2Er0.2Tm0.2Sc0.2)2Si2O7: A potential environmental barrier coating material. *J. Eur. Ceram. Soc.* **42**, 3570–3578 (2022).
10. Perrudin, F. *et al.* Influence of rare earth oxides on kinetics and reaction mechanisms in CMAS silicate melts. *J. Eur. Ceram. Soc.* **39**, 4223–4232 (2019).
11. Ardrey, K. Thermochemical Degradation of Rare Earth-Based Environmental Barrier Coatings. doi:https://doi.org/10.18130/c3sd-xs90.
12. Ridley, M. Fundamental Degradation Mechanisms and Materials Optimization of Environmental Barrier Coatings. (2021).
13. Webster, R. I. & Opila, E. J. Mixed phase ytterbium silicate environmental-barrier coating materials for improved calcium–magnesium–alumino-silicate resistance. *J. Mater. Res.* **35**, 2358–2372 (2020).
14. Kane, K. A. *et al.* Steam oxidation of ytterbium disilicate environmental barrier coatings with and without a silicon bond coat. *J. Am. Ceram. Soc.* **104**, 2285–2300 (2021).
15. Richards, B. T. *et al.* Response of ytterbium disilicate-silicon environmental barrier coatings to thermal cycling in water vapor. *Acta Mater.* **106**, 1–14 (2016).
16. Leite, M. L., Degenhardt, U., Krenkel, W., Schafföner, S. & Motz, G. In Situ Generated Yb2Si2O7 Environmental Barrier Coatings for Protection of Ceramic Components in the Next Generation of Gas Turbines. *Adv. Mater. Interfaces* **9**, 2102255 (2022).
17. Gayler, M. L. V. Melting Point of High-Purity Silicon. *Nat. 1938 1423593* **142**, 478–478 (1938).
18. Sabooni, S., Karimzadeh, F. & Abbasi, M. H. Thermodynamic aspects of nanostructured Ti 5Si 3 formation during mechanical alloying and its characterization. *Bull. Mater. Sci.* **35**, 439–447 (2012).
19. Lee, K. N. Yb2Si2O7 Environmental barrier coatings with reduced bond coat oxidation rates via chemical modifications for long life. *J. Am. Ceram. Soc.* **102**, 1507–1521 (2019).

20. Bakan, E., Sohn, Y. J., Kunz, W., Klemm, H. & Vaßen, R. Effect of processing on high-velocity water vapor recession behavior of Yb-silicate environmental barrier coatings. *J. Eur. Ceram. Soc.* **39**, 1507–1513 (2019).
21. Gysi, A. P., Harlov, D., Filho, D. C. & Williams-Jones, A. E. Experimental determination of the high temperature heat capacity of a natural xenotime-(Y) solid solution and synthetic DyPO4 and ErPO4 endmembers. *Thermochim. Acta* **627–629**, 61–67 (2016).
22. KRSTANOVIĆ, I. Redetermination of oxygen parameters in xenotime, YPO4. *Z. Für Krist. - Cryst. Mater.* **121**, 315–316 (1965).
23. Hikichi, Y., Ota, T., Daimon, K. & Hattori, T. Thermal , Mechanical , and Chemical Properties of Sintered Xenotime-Type RPO4 (R=Y, Er, Yb, or Lu). **18**, 2216–2218 (1998).
24. Yunxiang Ni, Hughes, J. M. & Mariano, A. N. Crystal chemistry of the monazite and xenotime structures. *Am. Mineral.* **80**, 21–26 (1995).
25. Strzelecki, A. C. *et al.* Crystal Chemistry and Thermodynamics of HREE (Er, Yb) Mixing in a Xenotime Solid Solution. *ACS Earth Space Chem.* **6**, 1375–1389 (2022).
26. Bern, C. R., Shah, A. K., Benzel, W. M. & Lowers, H. A. The distribution and composition of REE-bearing minerals in placers of the Atlantic and Gulf coastal plains, USA. *J. Geochem. Explor.* **162**, 50–61 (2016).
27. Maciejewska, K., Szklarz, P., Bednarkiewicz, A. & Marciniak, L. Thermally-induced structural phase transition in rare earth orthophosphate nanocrystals for highly sensitive thermal history paints. https://doi.org/10.1016/j.jallcom.2022.168064 (2022) doi:10.1016/j.jallcom.2022.168064.
28. Wang, Y., Chen, X., Liu, W., Cheng, L. & Zhang, L. Exploration of YPO4 as a potential environmental barrier coating. *Ceram. Int.* **36**, 755–759 (2010).
29. Ushakov, S. V., Helean, K. B., Navrotsky, A. & Boatner, L. A. Thermochemistry of rare-earth orthophosphates. *J. Mater. Res.* **16**, 2623–2633 (2001).
30. Hetherington, C. J., Jercinovic, M. J., Williams, M. L. & Mahan, K. Understanding geologic processes with xenotime: Composition, chronology, and a protocol for electron probe microanalysis. *Chem. Geol.* **254**, 133–147 (2008).
31. Ji, Y., Beridze, G., Bosbach, D. & Kowalski, P. M. Heat capacities of xenotime-type ceramics: An accurate ab initio prediction. *J. Nucl. Mater.* **494**, 172–181 (2017).
32. Zhang, P. *et al.* Xenotime-type high-entropy (Dy $_{1/7}$ Ho $_{1/7}$ Er $_{1/7}$ Tm $_{1/7}$ Yb $_{1/7}$ Lu $_{1/7}$ Y $_{1/7}$)PO $_4$: A promising thermal/environmental barrier coating material for SiC $_f$ /SiC ceramic matrix composites. *J. Adv. Ceram.* **12**, 1033–1045 (2023).
33. Han, J., Wang, Y., Liu, R. & Wan, F. Theoretical and experimental investigation of Xenotime-type rare earth phosphate REPO4, (RE = Lu, Yb, Er, Y and Sc) for potential environmental barrier coating applications. *Sci. Rep.* **10**, (2020).
34. Zhao, G., Xu, B., Ren, K., Shao, G. & Wang, Y. Oxygen diffusion through environmental barrier coating materials. *Ceram. Int.* **46**, 19545–19549 (2020).
35. Ridley, M. J., Pinnisi, D. J. & Opila, E. J. Holistic comparison of environmental barrier coating material candidates through design of a figure of merit. *J. Am. Ceram. Soc.* **107**, 4405–4422 (2024).

36. Ridley, M., McFarland, B., Miller, C. & Opila, E. YbPO4: A novel environmental barrier coating candidate with superior thermochemical stability. *Materialia* **21**, 101289 (2022).
37. Majee, B. P., Bryce, K., Huang, L. & Lian, J. High temperature steam corrosion of LuPO4 and high-entropy rare earth phosphates in the presence of Al(OH)3 and Si(OH)4 impurities. *Npj Mater. Degrad.* **9**, 76 (2025).
38. Majee, B. P., Bryce, K., Huang, L. & Lian, J. A high-entropy rare-earth phosphate and its principle single component $REPO_4$ for environmental barrier coatings. *J. Adv. Ceram.* **14**, 9221041 (2025).
39. Bryce, K., Majee, B. P., Huang, L. & Lian, J. A systematic study of thermomechanical properties and calcium–magnesium–aluminosilicate (CMAS) corrosion of multicomponent rare-earth phosphates. *J. Adv. Ceram.* **13**, 1807–1822 (2024).
40. Wang, F., Guo, L., Wang, C. & Ye, F. Calcium-magnesium-alumina-silicate (CMAS) resistance characteristics of LnPO4 (Ln = Nd, Sm, Gd) thermal barrier oxides. *J. Eur. Ceram. Soc.* **37**, 289–296 (2017).
41. Majee, B. P., Bryce, K., Huang, L. & Lian, J. CMAS corrosion resistance of rare earth phosphates at high temperatures for environmental barrier coatings. *J. Am. Ceram. Soc.* **108**, e20251 (2025).
42. Wu, S. *et al.* Recovery of rare earth elements from phosphate rock by hydrometallurgical processes – A critical review. *Chem. Eng. J.* **335**, 774–800 (2018).
43. Krämer, S., Yang, J., Levi, C. G. & Johnson, C. A. Thermochemical Interaction of Thermal Barrier Coatings with Molten CaO–MgO–Al2O3–SiO2 (CMAS) Deposits. *J. Am. Ceram. Soc.* **89**, 3167–3175 (2006).
44. Kane, K. *et al.* Oxidation of 3D-printed SiC in air and steam environments. *J. Am. Ceram. Soc.* **104**, 2225–2237 (2021).
45. Stack, P. *et al.* Dry air cyclic oxidation of mixed Y/Yb disilicate environmental barrier coatings and bare silica formers. *J. Eur. Ceram. Soc.* https://doi.org/10.1016/J.JEURCERAMSOC.2022.02.009 (2022) doi:10.1016/J.JEURCERAMSOC.2022.02.009.
46. Coryell, C. D., Chase, J. W. & Winchester, J. W. A procedure for geochemical interpretation of terrestrial rare-earth abundance patterns. *J. Geophys. Res. 1896-1977* **68**, 559–566 (1963).
47. Taylor, S. R. The abundance of the rare earth elements in relation to their origin. *Geochim. Cosmochim. Acta* **19**, 100–112 (1960).
48. Eby, G. N. Abundance and distribution of the rare-earth elements and yttrium in the rocks and minerals of the Oka carbonatite complex, Quebec. *Geochim. Cosmochim. Acta* **39**, 597–620 (1975).
49. Lin, Y., Yang, Y., Dai, J., Zou, L. & Guo, L. High-entropy strategy makes rare-earth phosphates more suitable for use as thermal barrier coating materials. *Ceram. Int.* **51**, 59120–59129 (2025).
50. Qi Jun Hong *et al.* Ab initio molecular dynamics prediction and experimental validation of the 14:4 rare-earth oxide oxide-phosphate structure. *Proc. Natl. Acad. Sci. Submitt.*
51. SERRA, J., J, C., A, R., H, D. & G, G. ETUDE DES FAMILLES D'OXYPHOSPHATES DE LANTHANIDES (LN/P>1): SYNTHESE, CARACTERISATION ET STABILITE THERMIQUE. *ETUDE Fam. OXYPHOSPHATES Lanthan. LNP1 Synth. CARACTERISATION STABILITE Therm.* (1978).

52. Parker, C. G. & Opila, E. J. Stability of the Y 2 O 3 –SiO 2 system in high-temperature, high-velocity water vapor. *J. Am. Ceram. Soc.* **103**, 2715–2726 (2020).